SOFT ROBOTICS
Volume 6, Number 4, 2019

DOI: 10.1089/soro.2018.0080

SoRo
Soft Robotics

ORIGINAL ARTICLE

Turning in Worm-Like Robots: The Geometry of Slip Elimination Suggests Nonperiodic Waves

Akhil Kandhari,[1] Yifan Wang,[1] Hillel J. Chiel,[2–4] and Kathryn A. Daltorio[1]

Abstract

Inspired by earthworms, soft robots have demonstrated locomotion using segments with coupled length-wise elongation and radial contraction. However, peristaltic turning has primarily been studied empirically. Surface-dependent slip, which results in frictional forces that deform the body segments, makes accurate models challenging and limited to a specific robot and environment. Here, instead of modeling *specific* surfaces and segments, we take a geometric approach to analyzing the constraints that result from elimination of slip for the *general* case of peristaltic locomotion. Thus, our abstract two-dimensional model applies to many different mechanical designs (e.g., fluidic actuation, origami, woven mesh). Specifically, we show how turning is limited by segment range of motion, which means that more than one wave will be required to completely reorient the body in an environment where slip is not possible. As a result, to eliminate slip, segments must undergo nonperiodic shape changes. By representing segments as isosceles trapezoids with reasonable ranges of motion, we can determine control waves that in simulation do not require slip. These waves follow from an initial ''reach'' (i.e., kinematic movement range) of the second segment. A strategy for choosing the second segment reach is proposed based on evaluating long-term turn stability. To demonstrate the value of the approach, we applied the nonperiodic waveform (NPW) to our earthworm-inspired soft robot, Compliant Modular Mesh Worm with Steering (CMMWorm-S). With the NPW, the robot slips less when compared with a naive periodic waveform, where each segment of the robot has the same kinematic reach of each wave, as indicated by the difference between predicted and actual body position over multiple waves. Using an NPW for turning, we observe a decrease in prediction error compared with a naive periodic waveform by 66%. Thus, while our model ignores many factors (inertial dynamics, radial deformation, surface forces), the resulting turn strategies can improve kinematic motion prediction for planning. The theoretical constraints on NPWs that eliminate slip during turning will help robot designers make application-specific design choices about body stiffness, frictional properties, body length, and degrees of freedom.

Keywords: soft robots, robot kinematics, robot control, biologically inspired robots, soft robot turning

Introduction

Mobile soft robots inspired by earthworms[1–3] could have applications in medicine, search and rescue, and infrastructure inspection. Soft body locomotion[4–6] depends only on body deformation rather than the use of wheels or legs, which might break, slip, or get caught in tight spaces. However, to move in the desired direction, waves of extension and retraction must be coordinated as they travel along the body.[7] Currently, most worm robots work best traveling in straight lines on flat surfaces or completely constrained pipes. To make soft worm-like robots navigate in three-dimensional (3D) applications, a control theory for segment coordination during turning is needed.

A defining feature of earthworm-like robots is mechanical coupling between segment diameter and segment length.[8] When increasing diameter decreases length (and vice versa), this type of locomotion can be thought of as positive Poisson's ratio peristalsis (which we abbreviate as 3P). 3P coupling can be achieved either by a constant volume fluid

Departments of [1]Mechanical and Aerospace Engineering, [2]Biology, [3]Neurosciences, and [4]Biomedical Engineering, Case Western Reserve University, Cleveland, Ohio.

constraint (as in an earthworm's hydrostatic skeleton[9]) or by mechanical linkages (such as braided meshes,[10,11] pinned mesh rhombuses,[12–14] or curved springs[15]). Origami segments can have positive or negative effective Poisson's ratio, depending on the fold pattern.[16,17] Note that this analysis focuses on 3P structures; for a negative Poisson's ratio, however, the traveling waves would go in the other direction (from tail to head rather than head to tail for forward motion).[18] The advantage of 3P coupling is that it reduces the number of required actuators by mechanically linking the ground contact status of a particular segment of the body to the extension of that segment, as a single actuator is capable of causing an extension in length while contracting in diameter and vice versa.

In 3P locomotion, segments of the body that have the largest diameter (and thus shortest length) are the so-called anchoring segments.[7,18] The larger diameter anchoring segments press against the inner circumference of the pipe or against the floor. The smaller diameter segments do not contact at all. This is in contrast to some models of snake-robot crawling[19] where the weight is assumed to be supported evenly at all segments[20]—an assumption that may not be true in all animals.[21,22]

The frictional cost of transport (COT) for worm-like locomotion is determined by energetic losses to frictional slip.[20] Without the 3P constraint, the segments would not lift off the ground, and thus, all motion would require irreversible energy loss to sliding friction. As a result, the frictional COT (the work done against friction per weight and distance) would be equal to the friction coefficient[20] ($COT = E/mgd$, where the energy lost due to friction is defined as $E = \mu_k mgd$, m is mass, g is acceleration due to gravity, μ_k is the friction coefficient, and d is displacement), which can be high for a soft robot in a constrained space. However, we have recently shown that with 3P coupling and kinematic coordination, anchoring segments need not slip and thus the frictional COT can approach 0—similar to a rolling wheel.[12,23] For straight-line 3P locomotion, slip can be eliminated by coordinating the segments such that the rate of lengthwise elongation and retraction is equal between noncontiguous anchors.[7] Backward locomotion can be achieved by reversing the direction of the waves of elongation/retraction. For uneven ground, waves can be modified based on sensed ground contact forces[7,24,25] so as not to increase frictional COT.

Slip is a critical metric to minimize for several reasons. Uncoordinated control is not only inefficient but it can also be ineffective (e.g., the segments may change shape but not lead to robot progress). Slip can cause damage to delicate substrates (e.g., in medical applications). Furthermore, focusing on the geometric (kinematic) constraints is more generalizable to different robots and different substrate frictions than kinetic models (which will require stiffness, deformation, and contact force models).

To change direction without increase in frictional COT, slip-mitigating turning constraints need to be developed for worm robots, analogous to Ackermann steering constraints for wheeled robots. Current worm-like robots typically neglect this, often limiting control policy searches to periodic waveforms, and significant slip is observed.[10–12,15,26] Not only is energy wasted but also the motion is difficult to predict. In one example, with the same turning control policy, the robot's head moved *left* on high-friction surfaces and *right* on low-friction surfaces.[27]

The geometry of control for slip reduction provides a theoretical basis for control design, which can augment current approaches based on empirical trials,[28] genetic algorithms,[29] or fitting from animal data.[30] While rigid snake robots can be controlled for obstacle exploitation,[31,32] to similarly plan for worm-like robots, the 3P constraints should also be considered. This article demonstrates that without slip, multiple waves of nonuniform, nonperiodic control are required to change the body orientation for an abstract 3P robot. We call such control policies nonperiodic waveforms (NPWs). While other models of worm-like locomotion have focused on dynamics,[33] substrate compliance,[34] backward versus forward locomotion,[18] or contact-responsive timing,[7] to our knowledge, this is the first model to focus on the theory of slip reduction for turning gaits for a generic worm-like robot. In simulation, a general trapezoid model is developed and some turning strategies for anterior segments are provided as a first step toward developing full planning solutions for more detailed models.[35]

On our robot,[13] we show that by using kinematic constraints derived using this simple geometry, slip can be reduced using an NPW. Thus, NPW results in more predictable turning motions than the naive periodic waveforms we and others have used previously.[11,26–28] Specifically, kinematic models can predict the NPW-controlled position of our robot Compliant Modular Mesh Worm with Steering (CMMWorm-S) with positional error of less than 50% of the initial body diameter per cycle, whereas if a periodic wave is used, the positional error averages 160% of the body diameter per cycle. These positional errors are calculated by measuring the distance between the simulated trajectory and actual robot trajectory over 3 trials of 19 peristaltic cycles for each segment. The approximately tripled error in the periodic wave trials is due to forced slip and associated soft body deformation, which can be eliminated with the kinematic models presented in this article.

Model

We make some simplifying assumptions to develop a simple segment model with only two variables per segment (left- and right-side lengths) that will be applicable to different body designs such as those actuated with cables,[8,23] pneumatic pressure,[10,36] and shape memory alloy wires.[11,37] Note that the goal of the model is not to accurately describe all aspects of robot body motion in real environments, but rather to understand the general implications of imposing a no-slip constraint. We show in the subsequent sections that this simple model can contribute toward more predictable turning.

Assumptions

First, by assuming that each segment contacts the ground and anchors after retracting as much as possible, the body can be modeled in the two-dimensional (2D) plane of the turn (without calculating vertical positions of segments). We assume that the diameter of the body can be considered constant for the purposes of calculating distances between contact points. The 3P diameter decrease need only be enough to raise the moving body segments off the ground, and narrowing the diameter too much can result in excess bending due to gravity. For our robot, a decrease in diameter is coupled with an increase in length; however, even if the diameter decreases noticeably (as in Fig. 1, which is exaggerated), the

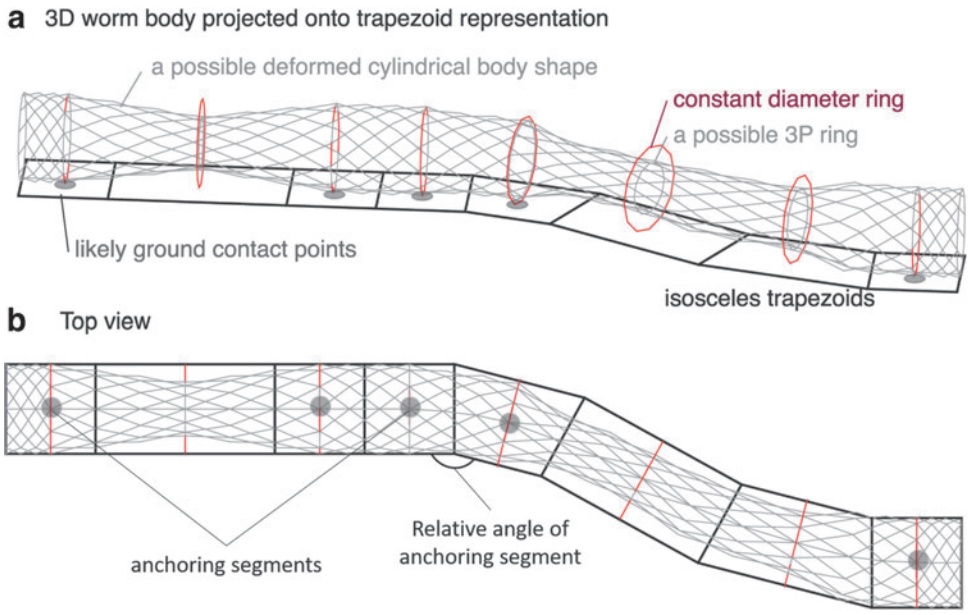

FIG. 1. A key property of worm-like 3P locomotion is that the short segments contact the ground, whereas the long segments do not. Here an example three-dimensional cylindrical mesh in which radial strain is −40% of longitudinal strain (Poisson's ratio = 0.4) is shown. At the center of each segment is a ring (*red ring*), which can change diameter slightly (*gray rings*) as the left- and right-side lengths change. The mesh shape shown is constructed with two intermediate rings along piece-wise arcs with interpolated diameters between each pair of actuated rings, connected in a helical pattern. The isosceles trapezoid projection is shown below. For our latest mesh robots, the minimum number of segments that can be raised off the ground is two adjacent turning segments and three straight segments. The remaining segments contact the ground beneath the actuators with shortest length, indicated with filled *gray circles*. In this article, the trapezoids around those points will be considered anchoring segments. 3P, positive Poisson's ratio peristalsis.

important part of the shape is the relative location and angle of the anchoring segments, which are affected less because the anchoring segment's diameter is larger. In other words, side lengths between variable diameter rings are approximated using side lengths between constant diameter rings. A more accurate model would require an expression for the length/diameter coupling relationship (which might be nonlinear for a particular robot) as well as appropriate intersegmental smoothing. Since the number of free parameters (right- and left-side lengths) would be the same, it is more general and simpler geometrically to use the isosceles trapezoid segments here with leg length equal to the nominal diameter. Later work may include a transformation into more robot-specific quadrilaterals.

The second simplification is that the effect of the actuators can be modeled independently from each other. In other words, for our worm-like robot, contraction of a segment affects the dimensions of adjacent segments (Fig. 1). We have shown, however, that when the body is a continuous mesh, the actuation effects can be linearized and separated into independent local changes,[38] and thus, the body can be considered in discrete segments for the purpose of control.

This model applies to other actuation schemes for 3P segments that both elongate and bend. In this article, we refer to the soft body as turning left or right, but this model can also be applied to other directions (e.g., vertical bending to climb up walls).

Trapezoid segment model

The relationship between basis length and bending angle β can be found with geometry. Each segment is a trapezoid with left-side length w_L, the right-side length w_R, and the trapezoid legs are the constant diameter d, as shown in Figure 2. Thus:

$$\frac{1}{2}(w_R - w_L) = d\cos\beta \tag{1}$$

A trapezoid representation of the body is exact if the centerline follows a series of piecewise tangent arcs at the actuator. Note that trapezoids are a more convenient representation because, in the default straight positions, they have equal base side lengths rather than the infinite radii of curvature. When finite, the radius of curvature for the center

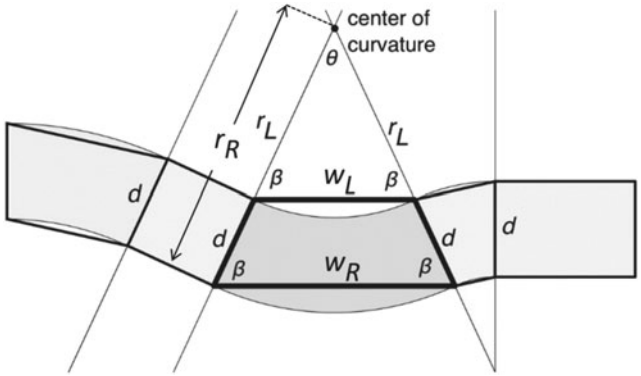

FIG. 2. The body of a worm-like robot is represented using a series of trapezoids (*heavy lines*), which could alternatively be represented using a series of arcs (*shaded gray*). w_L and w_R are the leg lengths and d is the nominal diameter.

(midpoint of diameter d) is the average of the left and right curve radii (r_L and r_R). The curve radii are related by geometry to the trapezoid parameters by the following:

$$|r_L - r_R| = d$$

$$r_L \cos\beta = w_L/2 \tag{2}$$

$$r_R \cos\beta = w_R/2$$

The included arc angle, θ, of each of these curves also defines isosceles triangles as shown in Figure 2. Since the sum of all the included angles in a triangle is equal to 180°:

$$\theta/2 + \beta = 90^\circ \tag{3}$$

The limits of segment deformation will have important effects on the way the robot turns. To better visualize deformation, here we allow the segment to elongate to 100% of its initial length. Furthermore, the initial short segment length is set equal to the nominal diameter. Thus, after normalization by the diameter, the initial configuration of a segment is the 1×1 square at the lower left corner of Figure 3 and we assume each segment can be controlled to achieve any of the trapezoid shapes within the bounds in Figure 3. These bounds were determined by extending one side (left or right side) of a single segment of our worm-like robot, CMMWorm-S, while keeping the other side length constant and measuring the side lengths of the segment. The configuration space represents the dimensions a single segment of the CMMWorm-S can achieve, normalized by diameter.

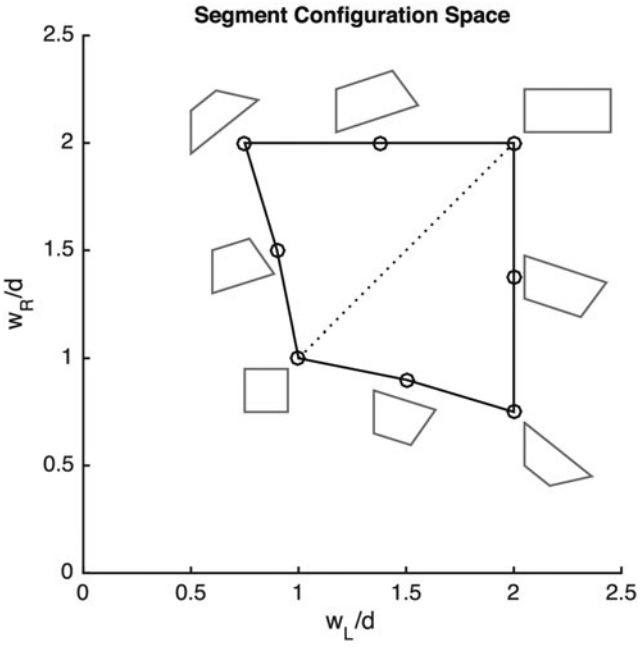

FIG. 3. A worm-like robot, like our robot CMMWorm-S, will have limits on the possible shapes of a single segment. For the simulated examples shown here, the trapezoid segments must be within these bounds, which are generous for the worm robot, as given in Kandhari *et al.*[13] Diagrams of the trapezoids represented by the *boundary dots* are shown near the border. w_R/d and w_L/d are the right and left trapezoid base lengths, respectively, normalized by diameter.

Problem scope

This model is used to search for control waveforms that balance elongation and retraction of segments such that slip motions at the anchoring segments are not generated. Specifically, we focus on waves for which two segments are moving at once (one elongating and one retracting). This type of wave is referred to as a 2×1 NPW,[8] where, as a segment is extending in length, an adjacent segment is shortening in length. In our robots, increasing the number of segments per wave (e.g., 3×1 with a suspended segment between contracting and retracting segments) can cause some segments to drag along the ground when extended. For expediency, subsequent waves can begin before the first wave reaches the end of the body (e.g., 2×2 waves),[8] but for clarity here only one wave at a time is shown on the body.

Implications of NPWs

First, this section demonstrates that slip elimination control (SEC) for straight-line locomotion can be achieved with symmetric periodic waves, as we have previously used. However, we show that, for turning, SEC may not result in straightening the body after a single wave, and waveforms need to change as they travel along the length of the body. Such waveforms will need to be calculated via the method of the next section based on the changing robot configuration and are hence referred to as NPWs.

The special case of straight-line motion

Straight-line 3P forward locomotion is achieved with waves of elongation and retraction that travel in the opposite direction as the moving robot. As a given segment elongates, a posterior segment retracts at the same rate, increasing the average progress of both segments. Thus, the SEC constraint of no-slip condition is satisfied as long as elongation and retraction rates between anchoring segments are equal.

Furthermore, because the elongating segment can elongate until it reaches the starting length of the paired retracting segment, and vice versa (Fig. 4A), the same waveform can be applied to the next pair of segments. In other words, the control waveform need not change as it travels down the body. Moreover, this is true for all segments after a wave passes down the body. As a result, subsequent waves can be identical to the initial wave. Next, we show that these waveform properties do not hold for all turning waves, for example (Fig. 4C), when the posterior and anterior segments of the body are oriented at 90° from each other, although they can hold for the special case of turns in which the body lies along an arc with constant radius (Fig. 4B).

A single NPW may not be able to reorient a straightened body to face a new direction in the same straight configuration

A key characteristic of the bending of the robot is how much a single wave can change the orientation of a segment. We consider this for the first segment of the robot from an initially straight configuration. Subsequent segments will follow the same pattern, that is, for some positions of the

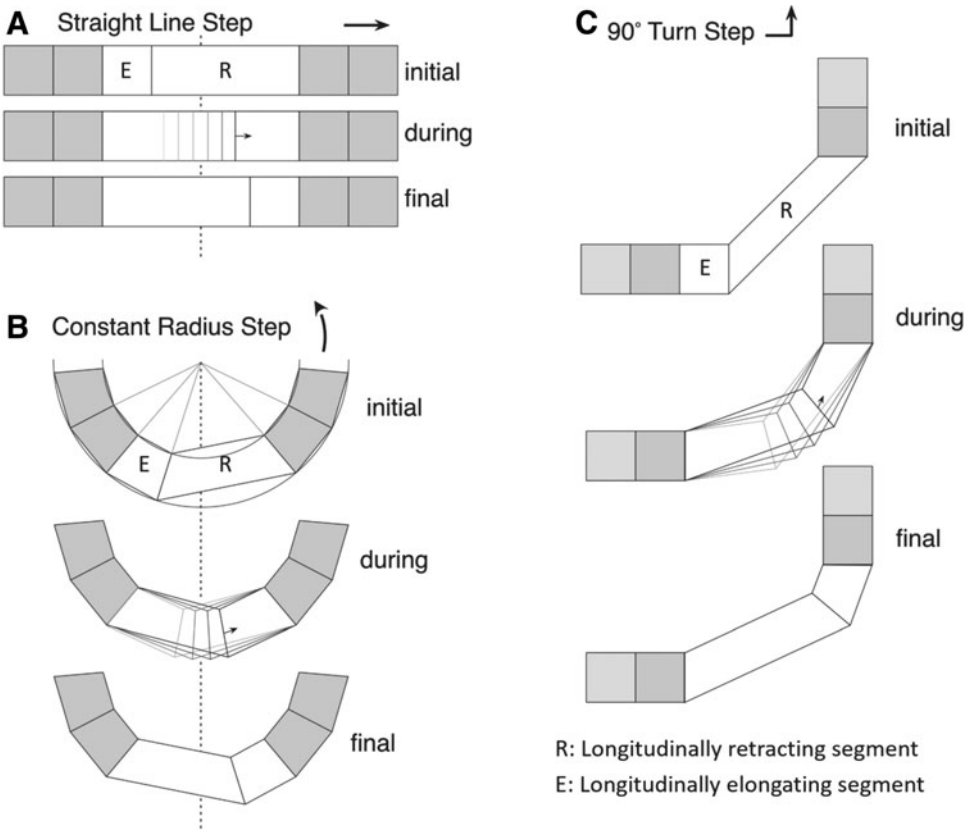

FIG. 4. Balancing a pair of elongating and retracting isosceles trapezoid segments (*white*) such that the anchoring segments (in *gray*) do not move. *Arrow* on top indicates direction of motion. Segments marked *R* are retracting in length, while segments marked *E* are elongating in length. A pair of segments retracting and elongating in length are shown for **(A)** straight-line motion **(B)** when the body lies along an arc with constant radius, **(C)** when the posterior and anterior of the body are oriented 90° from each other. The *gray* segments are anchoring segments and do not move as the retracting and elongating segments change states.

anterior segments, geometrically reachable positions required from the posterior segments might fall outside of their respective reachable space, which will cause these segments to slip.

When the first segment returns to its shortest shape and contacts the ground, the configuration of the second segment (the second segment ''reach'') will determine the contact position of the first segment, that is, the center point of the front of the first segment. The reachable space of the first segment from an initially straight configuration with a two-segment wave is shown in Figure 5.

After the first segment is at its maximum diameter, it becomes an anchoring segment and the third segment can begin extending while the second segment contracts. Thus, subsequent segments will be able to reach a translated reachable space by extending from their posterior anchoring segments (until the last two segments that can be cantilevered).

If we want to reorient the robot, that is, have it facing a different direction in the same straight configuration as the original, we can determine the necessary location of each segment by measuring backward from the front segment's initial reach. However, if that location is outside the translated reachable space for that segment, an anchoring segment will have to slip. In our example, the x-y reachable space limits eliminate many of the most extreme turns (black crosses, Fig. 6). However, even where the x and y coordinates of the required location lie within the reachable space, the orientation may not lie within the reachable configuration space. In fact, the orientation constraints interfere for all but the straight-line motions. This would mean that a point (e.g., a small foot) at the center of the segment might be able to stay in the same place for initial reaches that are represented by red dots in Figure 6, but that point and the body around it would have to rotate.

Thus, especially for long soft bodies, such as worms, or for segments with limited range of motion, there will not be an SEC wave that can completely reorient the straight body. In other words, the configuration of the posterior segments will require the reach of these segments to be outside their respective reachable kinematic configurations, hence necessitating slip. If slip is not permitted or possible, after one wave, the body will be in a different shape for the next wave.

Except when the body has uniform constant curvature, SEC waves will change as they travel down body

If the final shape of the retracting segment is the initial shape of the elongating segment (and vice versa), there is a symmetry that simplifies the control waveforms (as in straight-line locomotion). Because the relative geometry is the same before and after the wave has passed, subsequent waves can be identical to the first wave. However, this is only possible if the two outer edges of the elongating and retracting segments are mirror symmetric. If they are not mirror symmetric, as in Figure 4B and in Figure 7A and B, the initial and final relative positions of the anchoring segments will be different, necessitating slip. Note that not every mirror transformation corresponds to a pair of possible segments. In Figure 7C, a line of symmetry was found but the associated segment pair is not a trapezoid, and outside the segment configuration space.

In order for the first and last segment shapes to match without slip, both trapezoids in the moving pair must have the same center of curvature point (and therefore the same radii), and that center of curvature must lie on the mirror symmetry

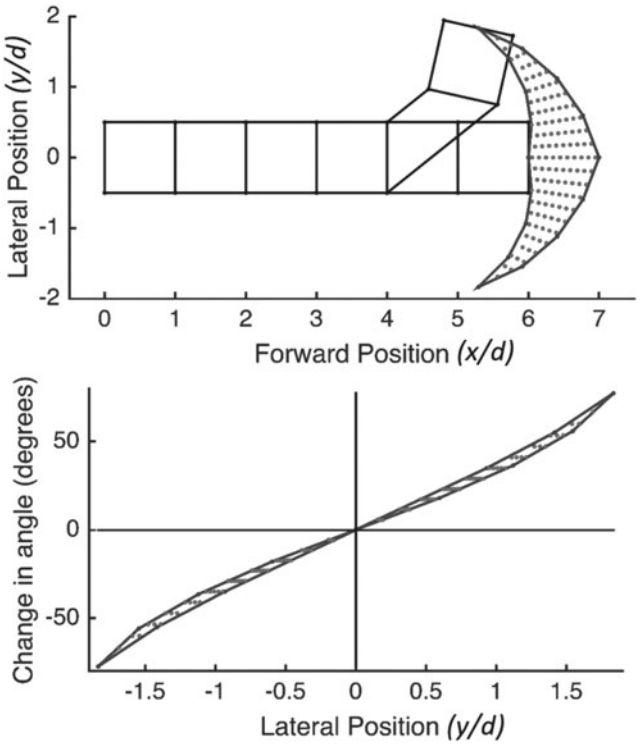

FIG. 5. The reachable space of the front segment assuming only two segments can be cantilevered off the ground, and the range of motion of a segment is as described by the configuration limits in Figure 3. The reachable space has three dimensions (x and y position, and angle). Two projections of this space are shown: (*top*) x and y and (*bottom*) y and angle turned by the first segment due to the kinematic reach of the second segment. Both x and y positions in (*top*) and (*bottom*) are normalized by diameter and hence are dimensionless.

line, as in Figure 7D. In this case, the short and long trapezoids will have a different included arc angle, θ (Fig. 8, where $\theta_1 \neq \theta_2$), which can be gradually equalized and then reversed without requiring anchor segments to slip. A consequence of this constraint is that there is no matched pair of trapezoids that includes exactly one rectangle: either both trapezoids must be rectangles or neither can be rectangles. If segment one (S_1) is a rectangle (A) and segment 2 (S_2) is a nonrectangular trapezoid (B) at the beginning of a wave, it will not be possible for S_2 to have shape A and S_1 to have shape B at the end of the wave.

As the wave travels down the body, this mirror symmetry must be true for each pair of anchors if subsequent waves are to be identical. For example, in Figure 7D, the second and fifth segments are mirror symmetric (while the third segment contracts and the fourth expands), but when the wave moves to anchor the third and sixth segments, they are not mirror symmetric. As a result, there exists no constant-shape phase-shifted traveling wave (periodic wave) that can reorient rectangular segments in one orientation to rectangular segments in another orientation.

This reveals a second special case of locomotion—if and only if all the segments in the body have the same center of curvature point, the SEC waves can be repeated identically and do not need to change amplitudes as they travel down the body. Just as the total of the two lengths remains constant as one increases and the other decreases for straight-line locomotion (Fig. 4A), the total of the two arc angles remains constant in a constant curvature turn (Fig. 4B). At every intermediate position, a trapezoid is defined by one segment with an increasing arc angle and one with a decreasing arc angle.

NPWs must be used to eliminate slip for nonconstant curvature turns. For example, NPWs are necessary when transitioning from a straight line to a turn or in the middle of a turn, when some segments are straight, as in Figure 4C. Such nonperiodic SEC waves are described in the following section.

Calculating SEC Waves

As the geometry above shows, SEC waves for arbitrary body configurations will be a function of the changing body shape: different for each wave in time and for each segment in the body. The front and rear segment waveforms are the least constrained since they have anchors only on one side during elongation and retraction. Here, they are elongated slightly and returned to square initial conditions. The nontrivial calculation of SEC waveforms begins at the second segment.

As described above, the initial second segment ''reach'' defines the anchoring position of the first segment. The choice of initial reach is described below.

Between anchoring segments, the moving segments are controlled such that the anchoring segments do not need to slip. We formulate the problem as determining four degrees of freedom (w_{R1}, w_{L1}, w_{R2}, and w_{L2}) such that the anchoring segments are stationary. Formally, the black dots in Figure 8 maintain their positions by satisfying the following three constraints:

1. The total length of the two trapezoids, s_L, in Figure 8, must be constant over time. Applying the cosine rule to the triangle defined by the left bases of the trapezoids and the line between them:

$$(s_L)^2 = (w_{L1})^2 + (w_{L2})^2 - 2w_{L1}\, w_{L2} \cos B \qquad (4)$$

where B is the angle between the bases of the adjacent trapezoids ($\beta_1 + \beta_2$) and $(s_L)^2$ is constant.

2. The total bending angle of the two trapezoids (angle Ω in Fig. 8) is constant.
3. The relative orientations of the two anchoring segments must be constant. Thus, the sum of the included arc angles $\theta_1 + \theta_2$ in Figure 8 must be constant. Since the isosceles triangle that corresponds to each isosceles trapezoid must have interior angles that sum to 180°, a constant $\theta_1 + \theta_2$ implies a constant $\beta_1 + \beta_2$.

With four degrees of freedom and three constraints, there is a 1D set of solutions. Thus, from one trapezoid base (e.g., w_{L1}, which would start from an initial position and increase until a stopping condition is reached), the other three (w_{R1}, w_{R2}, and w_{L2}) can be uniquely determined.

First, to get w_{L2} from w_{L1}, Equation (4) can be solved using the quadratic formula. The values of the constants s_L and B can be inserted from the starting conditions. Then, the individual trapezoid acute angles β_1 and β_2 can be found through

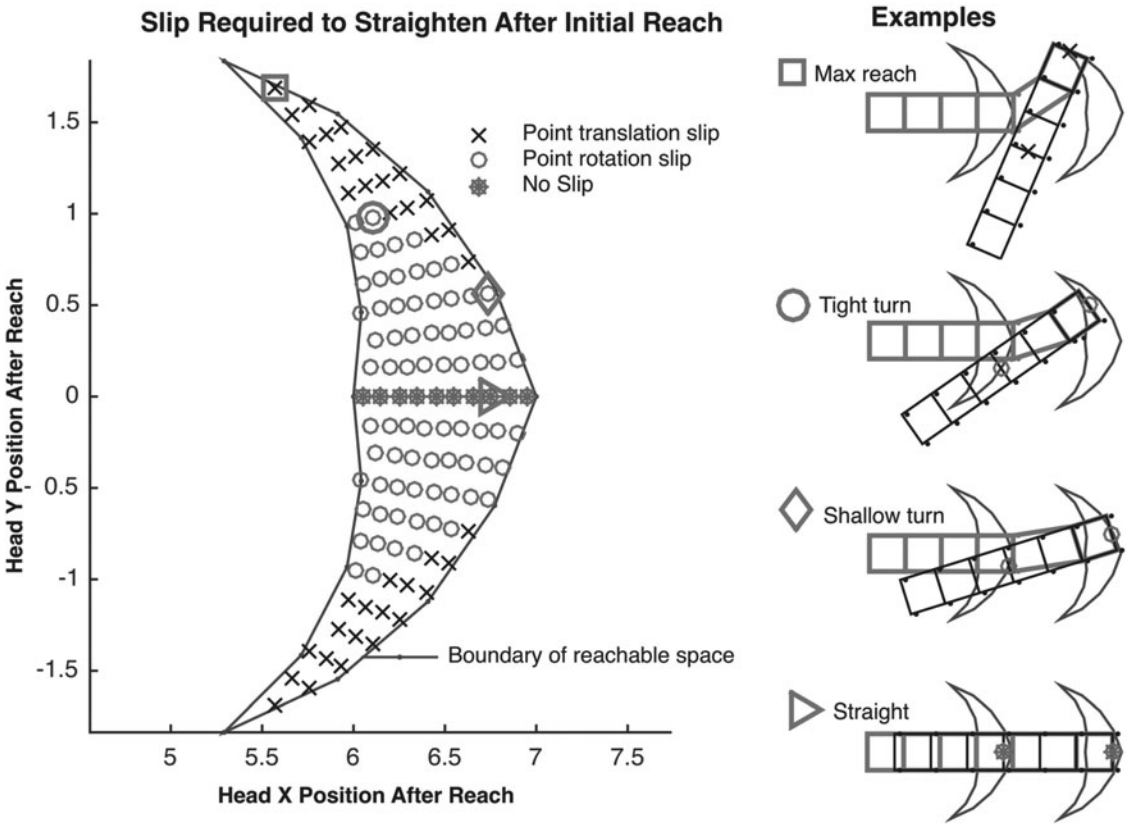

FIG. 6. Some areas of the reachable space do not permit the body to straighten out again after one wave without slip. In particular, slip without rotation is only possible for essentially straight-line motion. Schematics shown at right demonstrate how straightening the segments after choosing different points for the first segment reach, within the configuration space, will cause posterior segments (third segment in this case) to slip.

the sine rule because $w_{L2} \sin B = s_L \sin \gamma$, where $\gamma = \beta_1 - \Omega$, as in Figure 8. w_{L2} can be found from the following:

$$\sin(\beta_1 - \Omega) = w_{L2} \sin B / s_L \tag{5}$$

Once β_1 is determined from Equation (5), $B - \beta_1 = \beta_2$. Then Equation (1) can be used to find the right base lengths for the trapezoids (w_{R1}, w_{R2}). The choice of initial reach of the first segment, which along with initial configuration, determines all the constants (s_L, Ω, and B), and is discussed in the next section.

As shown for straight-line locomotion,[38] the rates of contraction and retraction can be estimated using Equation (4). Since the total length of the two trapezoids (s_L) must be

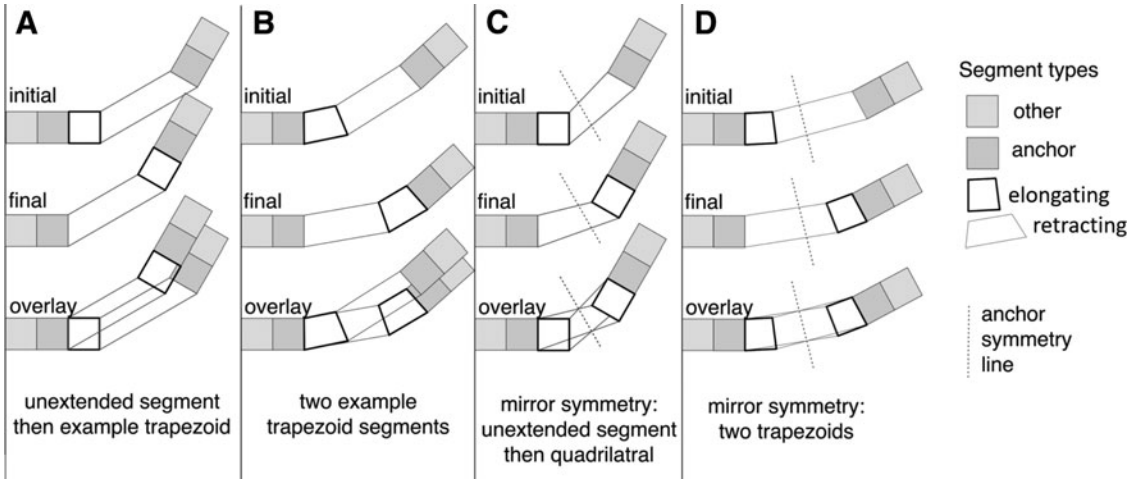

FIG. 7. If pairs of segments are controlled so that the short segment reaches the same shape as the long segment, and vice versa, it is clear from the overlaid initial and final configuration that slip will occur for **(A)** and **(B)**, but not for **(C)** and **(D)**, because of the mirror symmetry about the dotted line.

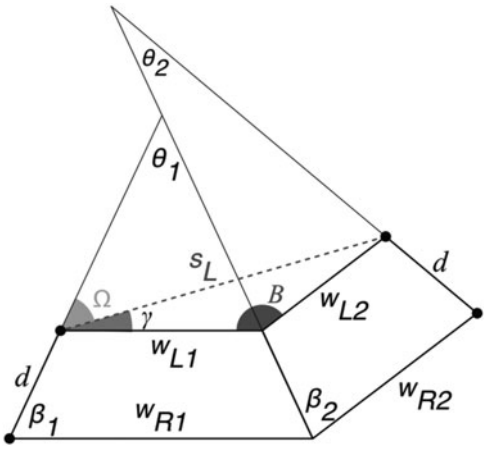

FIG. 8. A pair of trapezoid segments can move together, one elongating and one retracting, without necessitating slip of neighboring segments if the *black dots* do not move relative to each other. In the text, the geometry of NPWs is calculated from the parameters shown. NPWs, nonperiodic waveforms.

constant over time, taking the derivative of Equation (4), we can derive the rate at which the left-side lengths must change to keep the total length constant. On differentiating and simplifying, we derive the following relationship:

$$\dot{w}_{L1}(w_{L1} - w_{L2}\cos B) = -\dot{w}_{L2}(w_{L2} - w_{L1}\cos B) \qquad (6)$$

where $\dot{w}_{L1}$ and $\dot{w}_{L2}$ are the rate of change of left-side lengths of adjacent segments. $\dot{S}_L$ and $\dot{B}$ are zero since both of these values are assumed to be constant throughout a phase.

Note that the time dependence of these rates is based on actuation type, but the relationship between the rates, that is, Equation (6), remains constant.

Simulation Results

The result of these calculations is a set of NPWs that eliminates slip by coordinating pairs of actuating segments while keeping designated anchoring segments stationary. An example pair of segments is shown in Figure 9. This pairwise segment expansion and retraction will be extended to NPWs that travel down the body.

To generate the control wave for a whole body with a given initial shape, two design choices remain: the initial reach of the second segment (which determines direction) and the final conditions before transitioning to actuate the next pair (which determines segment step length). To permit as much motion as possible, the latter is determined by the limits of the configuration space (Fig. 9B). A portion of the resulting control is shown in Figure 9C.

Successive waves with the same initial reach

The control wave is uniquely determined by the actions of the front of the robot, specifically the reach of the second segment. First, we consider a simple control design that always uses the same second segment reach. In Figure 10, a

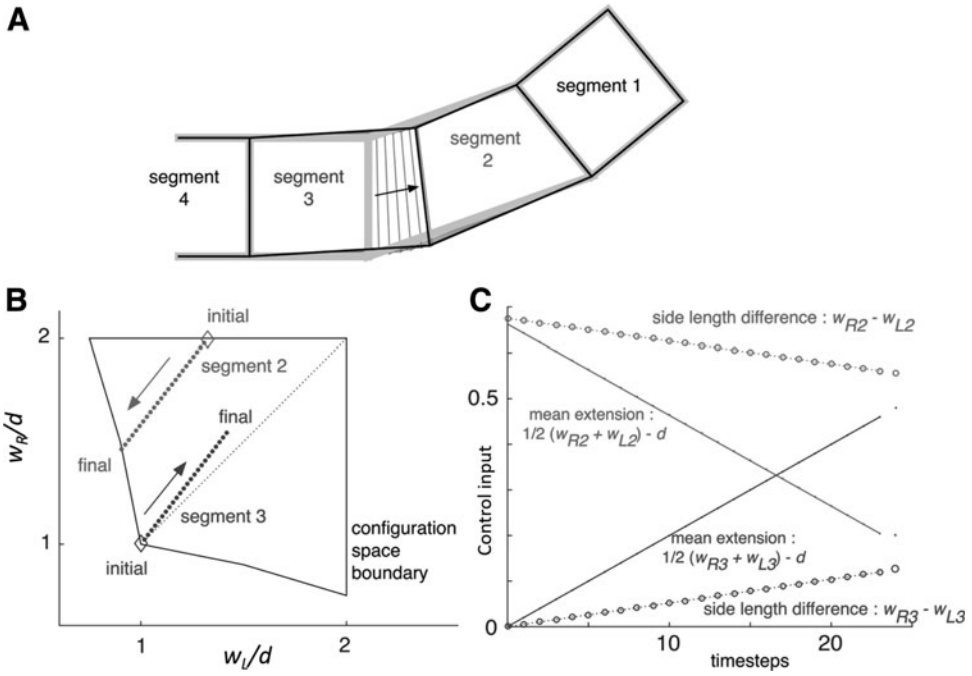

FIG. 9. **(A)** Diagram of paired extension and retraction with the initial configuration in *gray* and the final in *black*. The trapezoid side lengths of segments 2 and 3 are varied such that the only edge that moves is the one between segments 2 and 3. At each configuration during the transition, both segments 2 and 3 are isosceles trapezoids. **(B)** As viewed in the configuration space from Figure 3, the segments stop when one of them (in this case segment 2) reaches the boundary of the configuration space. **(C)** As viewed in the time domain, the mean extensions (the increase in length) intersect and the side length differences (a measure of the segment bending) change more gradually. Control input refers to the changing of the trapezoid lengths normalized by diameter (d); it is a dimensionless input that depends on the mean extension of the segment and the side length difference.

six-segment robot begins from a straight body configuration (six 1×1 squares), and a constant second segment initial reach is chosen. Four example initial reaches are shown: each left-side length is set to the maximum (two times the initial length), and the right initial side lengths are Figure 10A 0.9, Figure 10B 1.325, Figure 10C 1.6, and Figure 10D 2.0. Note that Figure 10D is the straight-line case where both side lengths are two times the initial length. In the first column, the shape of the body before and after a single wave is shown in thick gray and thin black lines, respectively. A small amount of progress is visible everywhere except the head (because the head progress occurred during the initial reach and was held constant during NPWs). If the same initial reach is chosen from that configuration and so forth for each successive configuration, the blue dotted path is followed. The second column shows the path and an example robot body over the first 100 waves. The converged shape of the path is shown in the third column.

As the examples show, a result of always choosing the same second segment reach over multiple waves can be either convergence to a constant curvature path (Fig. 10B, C) or a gradual decrease in motion magnitude ending in a stall in which subsequent segments cannot progress (Fig. 10A). The reason is that over multiple waves a navigation maneuver will change the body shape as well as its position and orientation. Since the magnitude of motion is limited by the initial conditions of each segment within the configuration space, the effect of the initial reach depends on body configuration. Thus, it is possible to choose a second segment initial reach that, in combination with the initial configuration of the third segment, permits little or no paired elongation and retraction between the second and third segments. In such a case, all the posterior segments will have nowhere to extend because they have reached the limit of their range of motion in the previous wave and the wave will be stalled (as a result, the blue and gray lines overlap exactly in Figure 10A, final column). To advance, another less extreme reach would have to be used at the second segment.

In Figure 10E, the entire space of possible initial reaches is explored. Three hundred waves were passed along an initially straight body to see the convergence properties of all possible combinations of left turning waves ($w_R \geq w_L$) at 0.025 resolution. The first panel shows how much distance the head moves at the 300th wave. The progress can be seen as the distance between the blue dots in the path of the robots in the above panels. The second panel shows the change in angular orientation after the 300th wave. The examples shown in the above panels are labeled as points on the right extreme of the plot.

This demonstrates that the stall conditions occur for turns that are too tight. Specifically, initial reaches that are within the dark blue triangle at the lower right of the range of motion decrease in progress over time.

Alternately, for many conditions, the segment configurations converge to a constant curvature path, which permits consistent turning. If the side lengths are nearly equal, greater progress per wave is possible with less turning (Fig. 10B). A middle strategy of extending one side length to about a midpoint of the range, while extending the other side length all the way, results in a stable reorienting turn (Fig. 10C, represented by the diamond in Fig. 10E).

Orienting to a desired direction

An important goal for steering a worm-like robot would be to orient to a particular direction. For example, the robot may need to follow a compass direction or a light source to find an exit. An efficient policy is needed that changes the body from traveling straight in one direction to traveling straight in another direction without turning too tightly (which can have diminishing progress per wave as is shown in Fig. 10A).

A solution is a stable reorienting turn combined with a head stabilization algorithm. As shown in Figure 11, to turn 90°, the example simulated robot used the initial reach from Figure 10C (long side extended to 2, short side to 1.325), until the second segment initial reach was able to orient the front segment to 90° from the original orientation. In this case, that new orientation occurred after seven waves. Subsequent initial reaches were calculated to always orient the front segment (the head) to face 90° while extending the second segment as much as possible.

FIG. 10. The nonperiodic SEC wave is determined from the initial shape of the second segment from the front (*light blue*) within the body (*gray*). The final shape after a single SEC wave (*black*) will advance the posterior segments as much as possible while holding the head stationary at that position. For a-d, x-axis indicates the forward position of the model normalized by diameter (*x/d*) and the y-axis indicates the lateral position normalized by diameter (*y/d*). The *blue* path indicates the progression of the midpoint of the front edge of the first segment. Each *column* shows the final orientation of the worm model after 1, 100, and 200 waves, respectively. For tight turns **(A)**, it is possible that continuing with the same reach results in smaller and smaller steps (as evidenced by *blue dots* spacing getting closer and closer and eventually stalling), whereas for other types of turns, **(B)** a stable reorienting turn and **(C)** a shallower turn, the path converges to a circular arc. The difference in the paths of **(B)** and **(C)** indicates a different trajectory followed due to different first segment kinematic reach. In straight-line locomotion **(D)**, the progress per wave is the greatest (as evidenced by the difference between the *gray* initial shape and *black final shape*). **(E)** Here we show the results of using the complete range of possible second segment reaches. The steady-state progress and turning of the above examples are shown within the context of the configuration space (long side length represents the trapezoid side that extends more longitudinally, whereas the short side length is the length of the shorter side of the trapezoid). It can be seen that below a certain line, progress will stall (region of zero progress in the *bottom corners*), for example **(A)**, represented by the *circle*. The fastest motion will be to walk in a straight line **(D)**, represented by an *upward triangle*. The fastest way to reorient will be at the maximum of the graph at the right (represented by the *diamond*). In the range between the two, trade-offs between forward progress and turning can be made [e.g., **(C)**, represented by the *left triangle*]. An initial reach with long side length less than two will result in smaller motions per wave. The first step for **(A)** takes into account the entire range of motion of the first segment based on the kinematic configuration of the second segment; hence, the turn made during the first wave is large. SEC, slip elimination control.

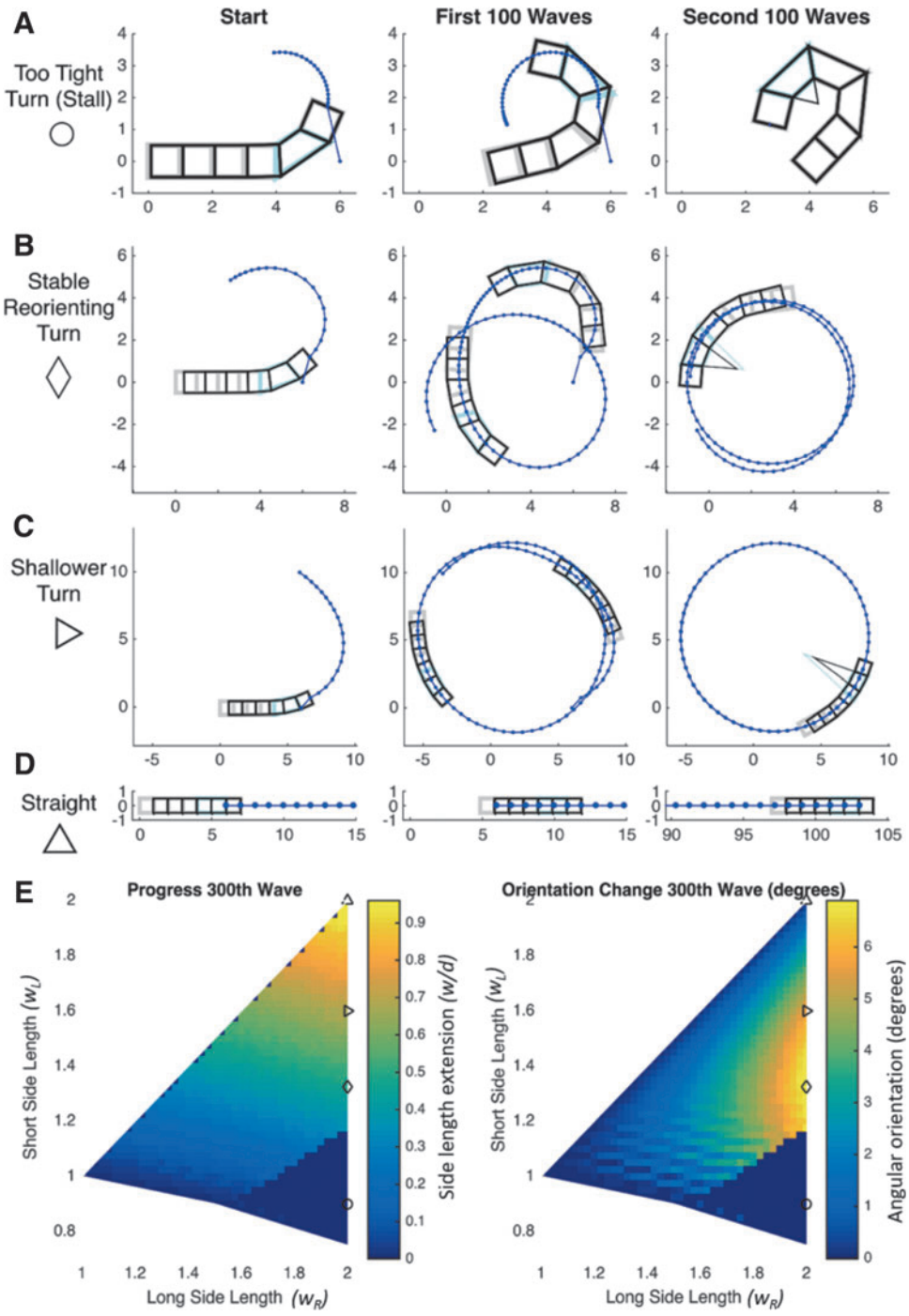

Specifically, the head stabilizing initial second segment trapezoid side lengths are calculated as follows. First, the difference in angle between the posterior edge of the second segment (α_{2p}) and the desired angle of the anterior edge (α_{2ad}) is determined. In our case, α_{2p} is measured from geometry of the trapezoid edge and α_{2ad} is 0° for a left 90° turn. The second trapezoid must have included arc angle, θ, equal to this difference. Using Equation (3), the included trapezoid angle, β, can be found from θ. Then from β, the difference in side lengths $(w_R - w_L) = \Delta w$ is found from (1). Thus, for a left turn, the second segment side lengths (w_{R2} and w_{L2}) can be found from the following:

$$\beta = 90^\circ - \frac{(\alpha_{2p} - \alpha_{2ad})}{2}$$

$$\Delta w = 2d \cos\beta$$

$$w_{R2} = w_{\max} \tag{7}$$

$$w_{L2} = \max(w_{\max} - |\Delta w|,\ w_{SRT})$$

where $d = 1$, $w_{\max} = 2$, and the stable reorienting turn side length is $w_{SRT} = 1.325$.

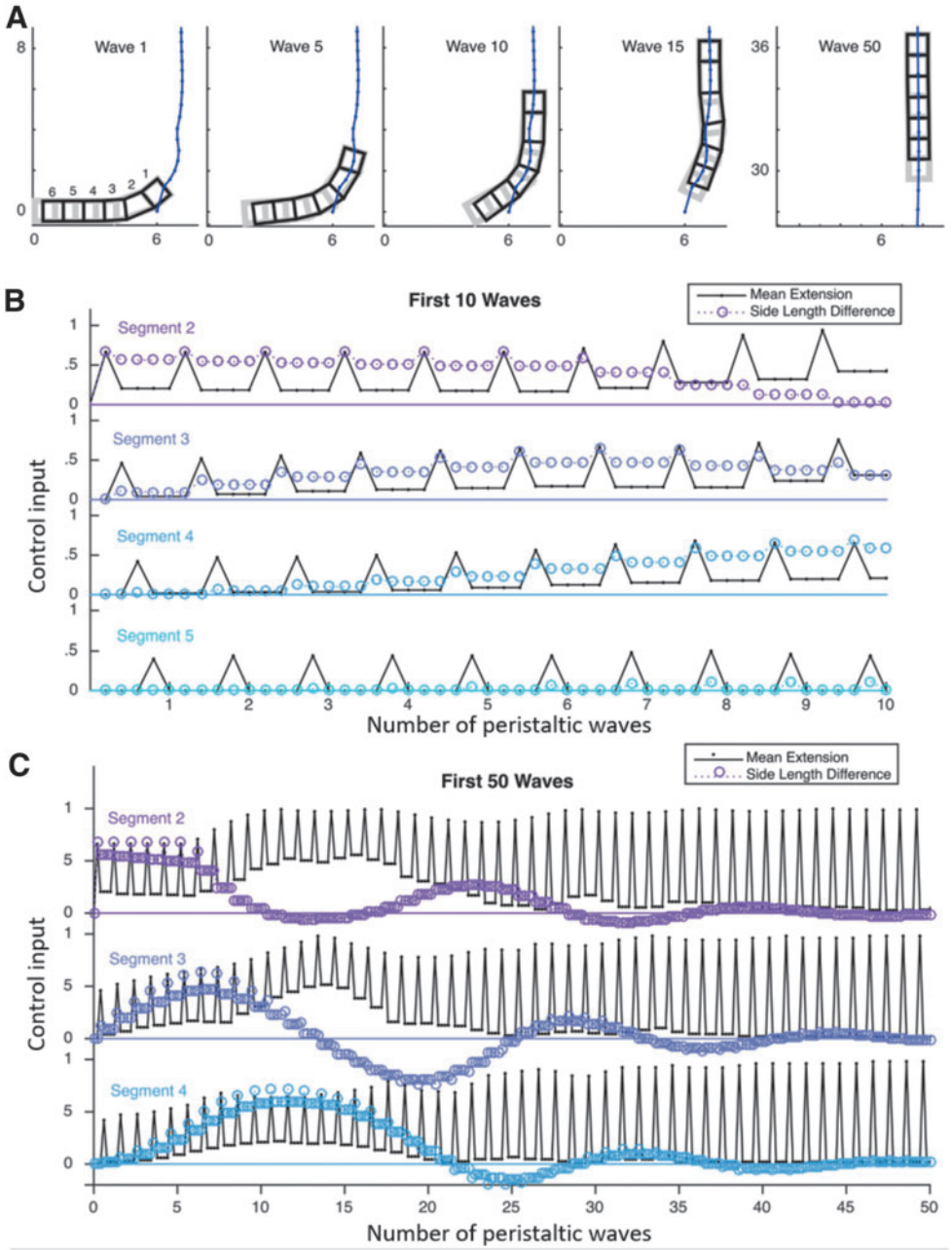

FIG. 11. An example simulation trial is shown with NPW control for a 90° turn ($\alpha_{2ad} = 0°$). **(A)** Starting with the initial reach determined above, and then, when possible, keeping the front of the robot facing parallel to the y-axis, the path of the robot and the initial and final states of the body for waves 1, 5, 10, 15, and 50 are shown. The SEC waveforms are shown **(B)** in detail for the first 10 waves and **(C)** over the full 50 waves. Control input refers to the changing of the trapezoid lengths normalized by diameter (d); it is a dimensionless input that depends on the mean extension of the segment and the side length difference. The *solid black line* is the mean extension of the segment's two side lengths $\frac{1}{2}(w_R + w_L) - d$ and indicates the elongation of the segment. Each segment of the body elongates and retracts once per wave. The amplitude of elongation gradually increases to the full limit of the range of motion. The *dotted lines* with *circles* are the difference in side lengths $(w_R - w_L)$, which indicate the bending of the segments. This changes more gradually, with damped oscillations that converge to zero when the body is straight at the new orientation.

A result of the SEC and range of motion limitations is that stabilizing to a new head orientation can take many waves. In our example, turning a six-segment worm by 90° can take over 50 peristaltic waves before all segments are reoriented toward the new direction. Aligning the front edge in a particular head direction requires that the x coordinate of the path varies slightly at first. Furthermore, to maintain a particular front segment angle, the body may have small bends or kinks. With this heuristic algorithm, after seven waves, the stable reorienting turn can align the head to face 90° from the original direction. After 15 SEC waves, the body is approximately aligned in the new direction and the path is straight. After 50 SEC waves, the kinks in the body straighten out and the motion converges to straight-line motion in the new direction.

Note that several other turning controls were tried (tighter turn steering, wagon handle steering, using smaller reaches [for which the right-side length was not at its maximum]); all these alternatives induced oscillations. The approach presented in Equation (7) is shown because it has a good balance of tight turning and smooth path (in blue), as shown in Figure 11A.

Robot Results

We validate the performance of the NPWs by applying them to an earthworm inspired soft-bodied robot, CMMWorm-S (Fig. 12).[13] CMMWorm-S is a cable-actuated, multisegmented soft robot. The locomotion of this robot depends on the material deformation of a series of flexible nylon tubes, held in a mesh configuration with 3D-printed vertex pieces. Even though the structure of this robot includes rigid components, the effective elastic modulus for the robot lies well within the range of soft robotics (0.5×10^4 Pascals).[13] In our previous article, we have shown that turning angle largely depends on the bending stiffness of the body, which is due to the flexibility of the nylon tubes used in the mesh.

Each segment of the CMMWorm-S is actuated using two actuators (Dynamixel AX-18A actuators) controlling either the left or right side of a segment. Each actuator controls a cable that runs along half the circumference of the segment. On actuation, cables are spooled in, contracting the segment in diameter and extending it in length. To produce turning motion, different cable lengths are spooled in by the two actuators within a segment, causing one side to extend more than the other, which in turn induces the robot to bend. The gait pattern can be changed by varying the longitudinal extensions of each side, based on the configuration space. The diameter of the robot ranges between 22 and 12 cm, depending on segment state.

Periodic wave to compare with NPW

We implemented the NPW on the CMMWorm-S robot and compared its performance with a naive periodic waveform, based on our previous published work.[13] For linear waves, we had defined a time-based control wave that involved two actuating segments (one extending in length and the other shortening) and traveled down the body one at a time (a so-called 2×1 wave).[8] To go straight, the extension and shortening rates were equal on left and right, keeping each segment left-right symmetric. To turn, we decreased the actuation speed on one side (from 70 to 18 rpm) for both extension and retraction. This causes segments to bend during actuation due to unequal spooling of cables on the left and right side of a particular segment. After longitudinal extension, the contracted segment expands in diameter until it returns to its initial anchoring state (maximum diameter). This pattern is the same for all segments, that is, all inner actuators rotate at 18 rpm and all outer actuators rotate at 70 rpm for 1.9-s duration, first in one direction and then in reverse. Thus, the control waveform is periodic (repeating for each cycle) and uniform (the same for each segment, phase shifted). This is a natural choice for a turning controller; however, as discussed in Kandhari and Daltorio,[27] significant slip is observed and whether the front of the body moved left or right depended on the surface friction.

We also simulated the periodic 2×1 waveform (Fig. 13) using isosceles trapezoids, using similar assumptions to the SEC model above. Unlike the NPW, the periodic wave has to slip at some point on the body and so we needed to add a slip assumption. Based on observations of the robot, the side of the robot with the fewest anchoring (max diameter) segments slips the most. For example, if segment one is an anchoring segment, segments two and three are a pair of actuated segments (segment two expanding in diameter and segment three contracting), and segments four, five, and six are anchoring segments, then to maintain the periodicity, segment one will experience slip. If there are the same number of anchoring segments at front and back, both sides are allowed to slip in a way that minimizes total slip (Fig. 13).

The NPW similar to Figure 11 was implemented on the robot with a few minor changes. The simulated model does not account for the motion of the first and last segments. Therefore, in the robot, the first segment was controlled to extend in length with maximum bias (difference between left- and right-side lengths) and the last segment was controlled to extend with zero bias (no difference in right- and left-side lengths) and 50% mean extension, that is, the left and right sides were extended uniformly to 50% of maximum extension. This allowed the last segment to be cantilevered and prevented it from dragging. Control input for segments two through five was based on the control input developed using the 2D model, as shown in Figure 11B. On the actual robot, the interconnected segments did not achieve the full range of motion in Figure 4 because of coupling between segments. Therefore, the waveform in

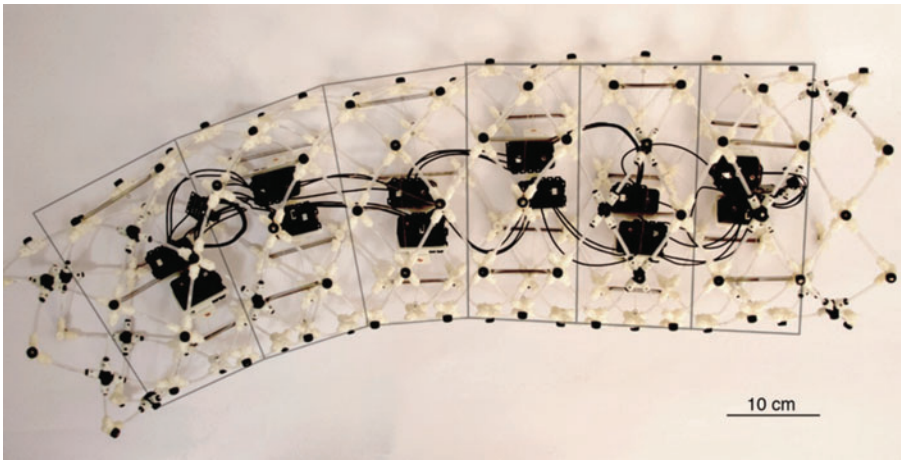

FIG. 12. Overhead view of Compliant Modular Mesh Worm with Steering[20] in a bent configuration. Schematic of six segments projected in the 2D plane is shown. Each segment includes two actuators (*black*) that change left and right segment side lengths. 2D, two-dimensional.

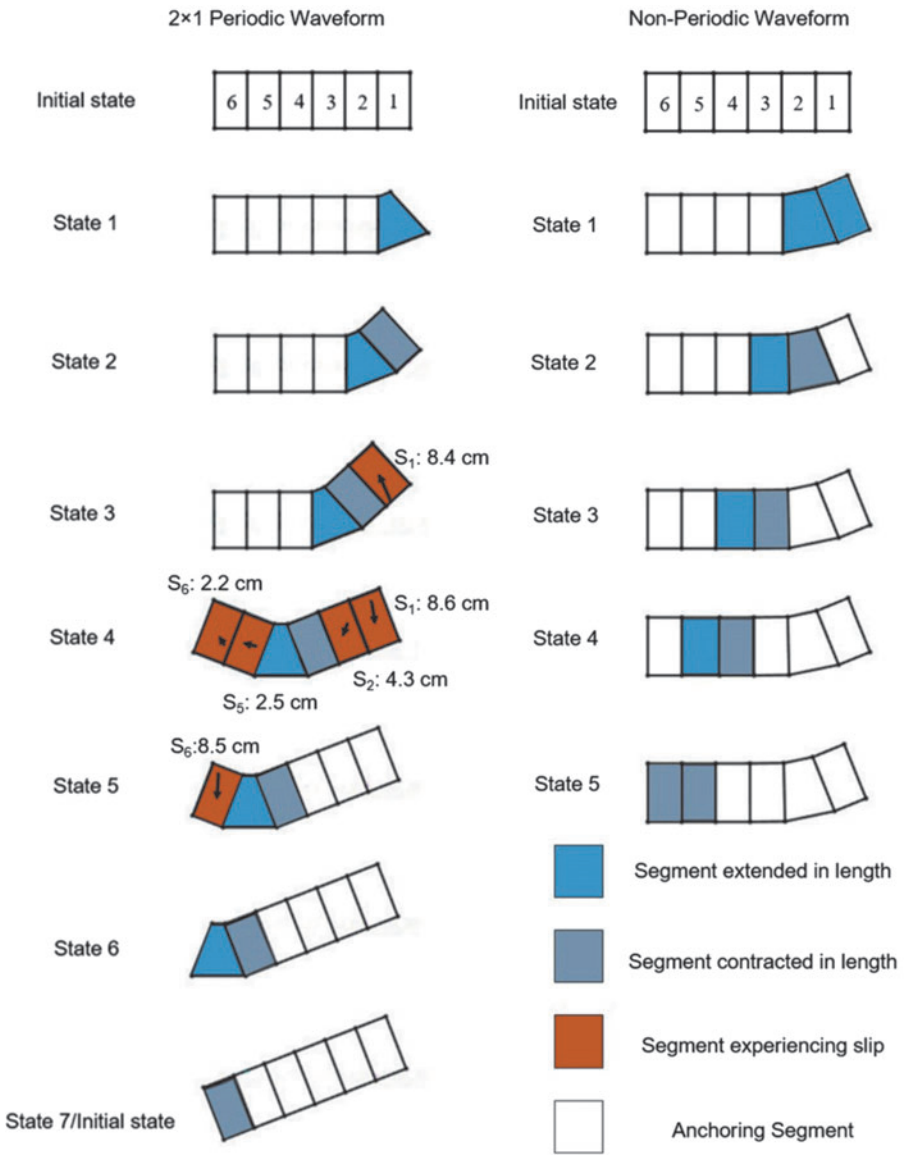

FIG. 13. Schematic extracted from the simulation for periodic 2×1 wave (*left*) and NPW (*right*). The robot in both cases is turning left. The segments of the robot are projected as isosceles trapezoids. For each state of the wave, a segment can be extending in length (*blue trapezoids*), contracting in length (*gray trapezoids*), or anchoring (*white trapezoids*). For a pair of actuating segments, longitudinal extension and contraction are constant for each state for periodic waveform and varies for NPW. For the periodic waveform, to maintain these shapes, some segments that are supposed to anchor must slip (*orange trapezoids*). For example, in state 4 of the periodic wave, no anchoring segment is present, since to achieve the configuration all segments experience slip. For the 2×1 wave, the segments that slip are shown in the figure and the corresponding distance experienced by a point (denoted by S_i, where i indicates segment number) that slips within a segment is shown. The *arrows* within the segments for periodic waveforms show the direction and magnitude of slip of the center of the segment from the previous state. The NPW shown is the first wave, starting from an initially straight position. Note that subsequent NPWs will have different initial configurations because the ending state and starting state are different and the segments do not expand to maximum diameter during expansion states.

Figure 11B was modified to accommodate a smaller amplitude wave. To calibrate this wave, a single segment was measured after different actuation speeds over the state duration (1.9 s). A linear regression was used to determine the actuation speeds to achieve the desired segment side lengths.

Robot experimental results

Experiments were performed for the two control policies (periodic and NPWs) on linoleum tile with a coefficient of static friction (μ_s) of 0.55. Videos from the overhead view were recorded for three trials of nineteen peristaltic waves each. Videos were analyzed using ImageJ (Version 1.51j8; National Institute of Health) and Tracker software (Version 4.11.0) to measure the angle turned by the robot after each peristaltic cycle while tracking the trajectory of each segment. Performance of the robot was measured by angle turned per peristaltic cycle and precision of the path followed by each segment of the robot compared with the path followed by the 2D models (Supplementary Videos S1 and S2

provided show the robot turning overlaid with the 2D model for periodic and NPWs).

We compared the angle turned by the robot with the predicted angle turned by the 2D model for periodic and NPWs. For simulation in both cases, the robot was targeted to turn by 90°; however, while testing, we limited the number of peristaltic waves to 19 instead of an angle-based endpoint. The angle turned is the angle between the original body orientation and the line segment between the first and last segment actuators after each cycle. After 19 peristaltic waves, the 2×1 periodic wave resulted in a turn of 76° in simulation and 57° on the robot. The NPW turned by 34° in simulation and 39° on the robot after 19 peristaltic waves. These results show that the angle prediction error is less for the NPW: with the NPW, the robot turned only 14% more than predicted, whereas with the periodic wave, the robot turned 25% less than predicted. Periodic waves, however, achieve a higher turning angle due to all segments turning with maximum capability, whereas for NPW, the segments are constrained to restrict any anchoring segments from slipping.

The trajectories for all six segments of the robot were tracked using Tracker, providing insight into segment slip that results in imprecise locomotion (Fig. 14). For simulated NPW (Fig. 14C), the segment trajectories overlap because the anchoring points are holding position. For the simulated periodic waves (Fig. 14A), the segment trajectories do not overlap but are spaced apart due to lateral slip, perpendicular to the direction of motion. In experimental trials of the periodic waves (Fig. 14B), the lateral slip tends to move the robot further in the opposite direction of the turn than predicted (i.e., the robot is turning right, but slip causes translation to the left). This translation is caused, in part, by the posterior segments tending

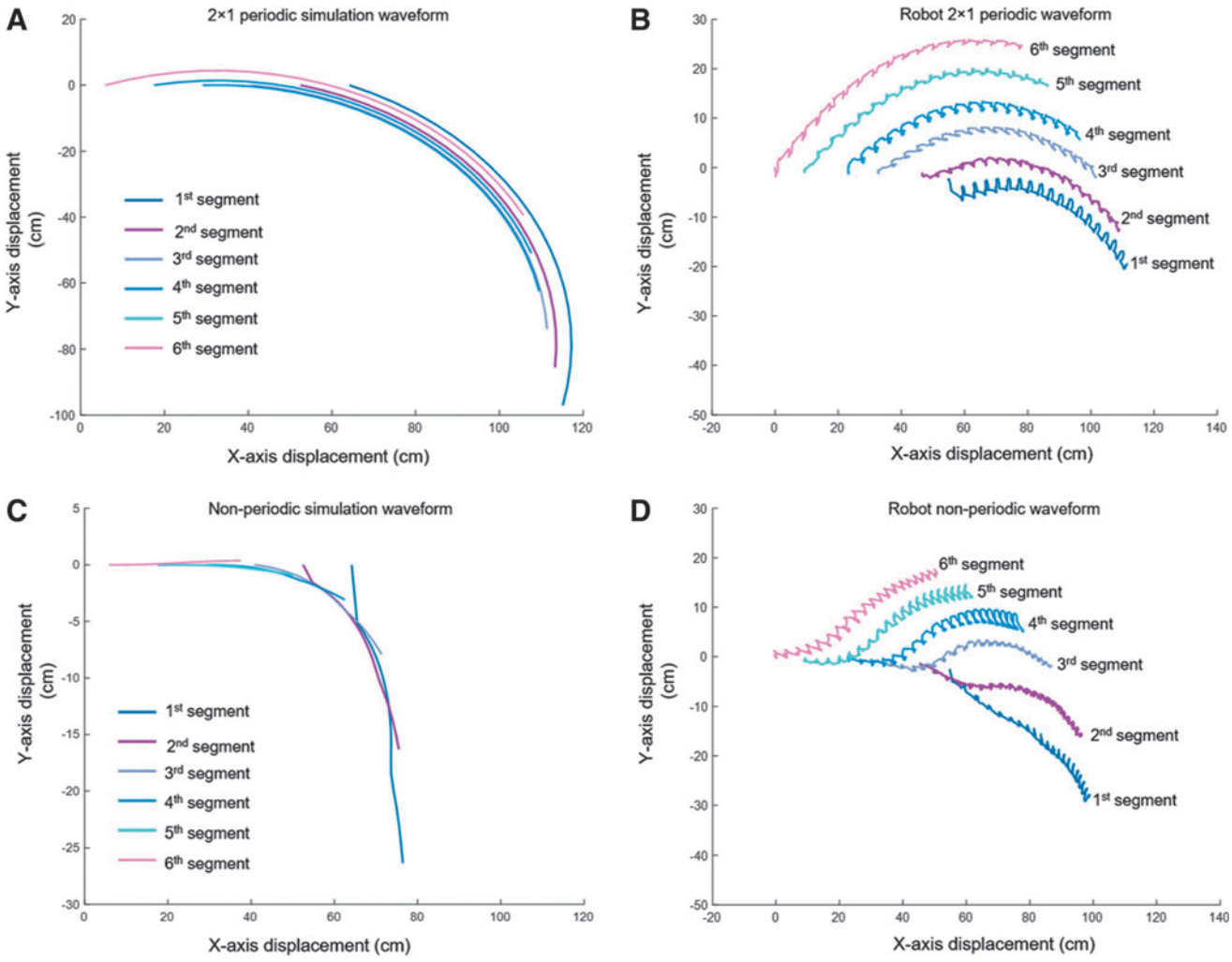

FIG. 14. Trajectories for each segment for **(A)** 2D periodic model, **(B)** robot using periodic waveform, **(C)** 2D non-periodic model, and **(D)** robot using NPW. **(A)** The model is allowed to experience minimal slip to maintain periodicity, and hence, each segment follows a trajectory that does not overlap with the trajectories of other segments. In **(C)**, the trajectories overlap, which is a necessary condition to eliminate slip using kinematic constraints. The trajectories from all six segments in **(B)** show that the trajectories do not overlap; rather, they experience a lateral slip (upward) instead of following the expected trajectory. For NPW in **(D)**, some trajectories overlap for brief periods, but the posterior segments experience more lateral slip compared with the anterior segments. The saw-tooth projections in **(B)** and **(D)** are caused when an adjacent segment is contracting or expanding circumferentially; due to coupling between segments, the neighboring anchoring segment moves [Supplementary Video S1 is used to plot the trajectories for **(C)** and **(D)**, and Supplementary Video S2 is used for **(A)** and **(B)**]. The axis limits are different for the plots for better visualization of the progress made.

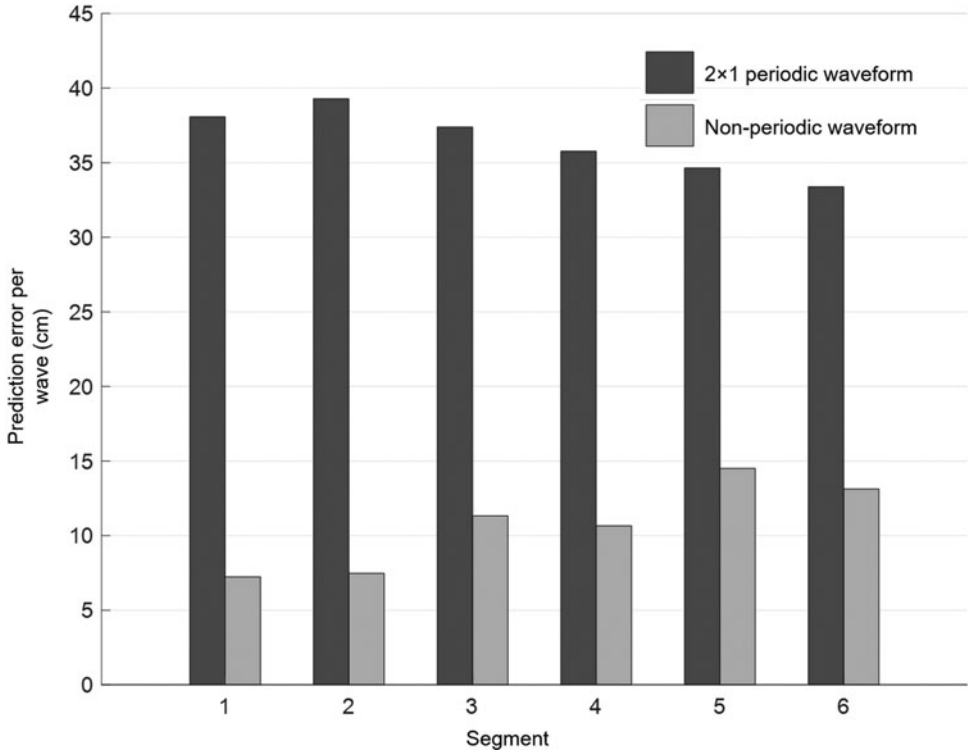

FIG. 15. For each of the six robot segments, the distance between simulation-predicted position and actual position at each state in Figure 13 is averaged over 3 trials with 19 wave cycles each. The NPW (*light gray bars*) has less prediction error (difference between model-predicted and measured segment location) than the periodic wave (*dark gray bars*), indicating less slip and thus more predictable movements for NPWs.

to ''whip out'' of their predicted trajectories, and then become anchors. In the NPW, this translation is less, as can be seen on the y-axis. After 19 peristaltic waves, the periodic wave moves left 20.4 cm, with an error of 80% relative to the predicted movement, whereas the NPW moves 29.16 cm, with a 13% error relative to the predicted movement. The asymmetric placements of the actuators along the length of the robot cause an uneven mass distribution between segments. During turning motion, this uneven mass distribution causes the robot to roll about its longitudinal axis. The lateral movements are amplified by the ability of the body to roll, which is not captured by the trapezoidal model. The robot trajectories show a saw-tooth motion. When we look at the details for a particular segment, we can see that the segment moves in different directions in the different phases, as shown in Figure 13. For example, in the fourth segment of the NPW, the predicted forward progress per wave starts out small and straight, but the anterior adjacent segments are turning. Because of the mesh structure, segments are not completely independent, unlike the simulation. This makes it difficult for the robot to achieve the desired SEC shape, which causes slip during anchoring. This slip is large relative to the progress during extension and contraction for the posterior segments, but smaller for the anterior segments.

We calculated the error between the actual robot path and the paths predicted with minimal slip (for the periodic waveform) or no-slip conditions (for the NPW). We compared the trajectories of the 2D model and actual robot data by recording the root mean squared error of the Euclidean distance between the center points of each segment after each wave (Fig. 15). Results show that NPW follows the predicted trajectory with one-third the total error of a periodic waveform (averaging 46% compared with 160% of the maximum segment diameter per wave). The posterior segments in NPW tend to have more error (37% of maximum segment diameter for front three segments and 55% of maximum segment diameter for rear three segments) than the predicted path, as observed in the trajectory in Figure 14. This is due to the end segment moving outward, as described above. For the periodic waveform, the overall error is more for all segments compared with the NPW. Posterior segments for the 2×1 periodic waveform, however, have less error when compared with the anterior segments (166% versus 150% of maximum segment diameter) because the front segments are required to slip more (as in Figure 13, segment 1 slips at minimum $8.4 + 8.6\,\text{cm} = 17.0\,\text{cm}$, whereas segment 6 slips $2.2 + 8.5\,\text{cm} = 10.7\,\text{cm}$).

Discussion and Conclusions

It might be naively assumed that a worm-like robot can be turned incrementally using an analytically optimal periodic wave. In this article, the geometrical analysis demonstrates that no such wave exists without slip—except for the trivial cases of straight-line locomotion or turning when the robot body is already bent in a uniform curvature arc. Neglecting slip in control design results not only in wasted energy but also in qualitatively different behaviors as a function of the substrate coefficient of friction.[26] This article analyzes the theoretical geometry required for slip elimination in planned worm-like robot paths.

For worm-like robots, simple path planning approaches do not apply. First, worm and snake-like robots are redundant (the number of independently actuated degrees of freedom (DOF) is greater than the state variables of the end effector), even hyper-redundant (because almost all the different actuators in a chain could advance the head in the same way, especially if friction is anisotropic).[39] Second, in some turning applications, the body shape in the environment matters as much as the head position. In that case, the combination of constraints (3P, SEC, and segment limits) leaves only two independently

controllable DOF of the robot (left and right initial second segment side lengths)—which means that the problem becomes nonholonomic (the number of state variables for the body, including configuration and position, is greater than the number of controllable DOF). Neither nonholonomic nor redundant robots can use traditional inverse kinematic manipulator planning, although there are computational approaches based on neural networks[40] or hierarchical optimization.[41]

The theoretical approach presented here may be valuable for path planning. The advantage of soft-bodied robots is to be able to go into challenging constrained places. Overhead motion tracking is unlikely to be available. We envision the robot having to traverse various terrains, possibly replanning as it goes. For example, to squeeze into a narrow tunnel from a smooth surface may require careful realignment of the body at a specific location. Being able to plan this motion can save power and decrease response time. Especially for many segmented worm-like robots, it would be wasteful and frustrating to have to back up and ''repark'' for small lateral translations. Since slip is unpredictable, understanding the constraints to eliminate it can improve accuracy of such plans. Understanding the reachable space, the types of possible paths, and the format of the necessary control waves is an essential first step.

This work shows how a turning worm-like robot can be modeled as a series of trapezoids (Figs. 1 and 2), which advance in pairs such that their neighboring segments are stationary anchors (Fig. 4). For a reasonable range of motion (Fig. 3), the reachable space of the head segment is determined (Fig. 5). However, for many of the points in that reachable space, slip is required for the rest of the robot to straighten out behind the head in a straight configuration because the straightened positions of subsequent segments are outside their own reachable spaces (Fig. 6). Thus, straightening in a new orientation without slip will require several control waves. Furthermore, when two moving segments are elongating and retracting, equivalent shape changes can be achieved without slip if and only if their edges are mirror symmetric and they share the same center of curvature (Fig. 7). Thus, unless all the segments on the body have the same center of curvature in initial and final configurations, the waves that control turning will not be phase-shifted periodic functions; rather, they will change as they propagate down the body.

This implies that rather than seeking a single waveform that can travel down the body and be repeated for subsequent turning, it may be valuable to consider a soft-bodied control strategy that is responsive to the body's configuration in the environment. The nominal control will be an NPW. Based on the geometric constraints (Fig. 8), these waves can be calculated (e.g., Fig. 9) from a particular choice of second segment reach. If the same reach is repeated, the motion either converges to a constant radius turn or stalls in a tightly curled shape (Fig. 10). To orient to a particular direction, head orientation stabilization can be used to calculate waves that converge to straight-line motion in a new direction (Fig. 11).

We applied the NPW to our soft-robot, CMMWorm-S (Fig. 12). For comparison, we also simulated and applied a periodic 2×1 waveform, which we expected to slip (Fig. 13). When the predicted and measured turn angle and body position (Fig. 14) are measured, we see that the robot in fact slips even more that the minimum amount predicted, which results in larger prediction error for the periodic wave than for the NPW control (Fig. 15).

We note that even though the NPW was calculated from a geometric ''slip elimination'' constraint, the robot can still be observed to slip relative to the theoretical position. For both periodic and NPWs, the robot experiences slip that the model does not capture. To accurately predict these slips, more detailed modeling may be required of both the robot and its environment. Continuous soft body modeling may account for segment inertia, interdependent soft deformation of adjacent segments, and segment diameter variation. Coulomb friction modeling, terramechanics, and new contact models are likely critical for modeling slip patterns on these and more diverse terrains. Such detailed robophysics models are making it increasingly possible to model and predict how a robot will behave on a particular surface.[42] These approaches can be important in correcting the specific errors that may accumulate along the body during turning locomotion.

In contrast to detailed physical modeling, the contribution of this article is a template that makes minimal assumptions about specific segment or environment kinetics. The goal is not to accurately predict slip (which requires assumptions specific to the robot and substrate) but rather to better understand how to reduce slip. Our work provides kinematic limits of peristaltic robots based on geometric constraints and an analytical control solution. Our robot results validate our approach by reducing slip. Despite imperfect control inherent in our imprecise robot, we can better predict the final location of the body with only 2D geometric models. Specifically, feedforward localization error of 46% of maximum segment diameter for NPW versus 160% of maximum segment diameter for periodic waves is a valuable improvement for following a desired path or arriving at a desired location.

In future work, this approach can be combined with more detailed models and feedback for even more accurate predictions. The robot still depends on some slip, which we can observe anecdotally from testing on high- and low-friction substrates. The experimental data illustrate imprecision of the open-loop shape controller due to segment-to-segment variation, load-induced deformation, coupling between adjacent segments, and 3D effects such as rolling (see Supplementary Videos S1 and S2), which has not been captured by the model. Nonetheless, when accurate segment loading information is not available, the robot experiments show that for our particular robot, the general model makes locomotion more predictable, by reducing slip.

The challenges in eliminating and predicting slip also provide a novel argument for controlling soft robotics with force control. We have shown how implementation of force sensors along the length of a worm-like robot can help reduce slip.[25] For turning, we envision force sensors to detect contact, which then determines anchoring segments. Between anchoring segments, where no forces are detected, segments can be controlled using Equations (1)–(5). If the direction of slip or shear surface forces can be detected, these baseline expansion and retraction rates can be altered to eliminate slip. Thus, this kinematic analysis is a critical step in achieving force control for peristaltic locomotion.

This article shows that in some cases, the slip elimination constraint may be too restrictive. For example, to turn quickly on a smooth hard surface, it might be better to design for lateral slip despite its energetic inefficiency and unpredictable dependence on the frictional coefficient. On granular media or in environments with nonlinear coefficient of

friction, slip elimination might not be desirable, as surface friction might prevent lateral motion needed to drag idle segments in such conditions.[42] In constrained environments (such as pipes), motion error might not be important. On the contrary, environments are not all the same and are continuously changing. Sometimes, paths will include both constrained and unconstrained passages, where predicting error can be important. NPWs may be called for in other applications such as (1) when following a desired trajectory is more important than turning speed, (2) when high substrate friction prevents slip, or (3) when the environment could be damaged by shear forces, as in medical applications. In these applications, understanding the limitations of SEC is essential for planning multiple waves to reach a desired location and configuration.

The geometrical analysis presented here establishes limits of possible no-slip behavior and will help robot designers relate segment range of motion and bending stiffness to slip requirements and turning speeds. In future work, we will be able to extend our modeling and control efforts to arrive at specific targets over a range of surfaces with varying frictional properties, with optimal cost or minimal number of waves.

Acknowledgment

Akhil Kandhari is funded by the National Science Foundation under NSF research award No. OISE 1844463.

Author Disclosure Statement

No competing financial interests exist.

Supplementary Material

Supplementary Data
Supplementary Video S1
Supplementary Video S2

References

1. Gray J, Lissmann HW. Studies in animal locomotion: VII. Locomotory reflexes in the earthworm. J Exp Biol 1938;15: 506–517.
2. Kanu EN, Daltorio KA, Quinn RD, *et al.* Correlating kinetics and kinematics of earthworm peristaltic locomotion. In: Conference on Biomimetic and Biohybrid Systems. Cham, Switzerland: Springer, pp. 92–96, July 2015.
3. Xu L, Chen HQ, Zou J, *et al.* Bio-inspired annelid robot: a dielectric elastomer actuated soft robot. Bioinspir Biomim 2017;12:025003.
4. Menciassi A, Gorini S, Pernorio G, *et al.* A SMA actuated artificial earthworm. In: 2004 IEEE International Conference on Robotics and Automation (ICRA). New Orleans, LA: IEEE, April 2004:3282–3287.
5. Umedachi T, Trimmer BA. Design of a 3D-printed soft robot with posture and steering control. In: 2014 IEEE International Conference on Robotics and Automation (ICRA). Hong Kong: IEEE, May 2014:2874–2879.
6. Kim B, Lim HY, Park JH, *et al.* Inchworm-like colonoscopic robot with hollow body and steering device. JSME Int J C Mech Syst Mach Elem Manuf 2006;49:205–212.
7. Daltorio KA, Boxerbaum AS, Horchler AD, *et al.* Efficient worm-like locomotion: slip and control of soft-bodied peristaltic robots. Bioinspir Biomim 2013;8:035003.
8. Horchler AD, Kandhari A, Daltorio, *et al.* Peristaltic locomotion of a modular mesh-based worm robot: precision, compliance, and friction. Soft Robot 2015;2:135–145.
9. Chiel HJ, Crago P, Mansour JM, *et al.* Biomechanics of a muscular hydrostat: a model of lapping by a reptilian tongue. Biol Cybern 1992;67:403–415.
10. Mangan EV, Kingsley DA, Quinn RD, *et al*. Development of a peristaltic endoscope. In: 2002 IEEE International Conference on Robotics and Automation (ICRA). Washington, DC: IEEE, May 2002:347–352.
11. Seok S, Onal CD, Cho KJ, *et al.* Meshworm: a peristaltic soft robot with antagonistic nickel titanium coil actuators. IEEE ASME Trans Mechatron 2013;18:1485–1497.
12. Boxerbaum AS, Shaw KM, Chiel HJ., *et al.* Continuous wave peristaltic motion in a robot. Int J Rob Res 2012;31: 302–318.
13. Kandhari A, Huang Y, Daltorio KA, *et al.* Body stiffness in orthogonal directions oppositely affects worm-like robot turning and straight-line locomotion. Bioinspir Biomim 2018;13:026003.
14. Mehringer A, Kandhari A, Chiel H, *et al.* An integrated compliant fabric skin softens, lightens, and simplifies a mesh robot. In: Conference on Biomimetic and Biohybrid Systems. Cham, Switzerland: Springer, pp. 315–327, July 2017.
15. Omori H, Nakamura T, Yada T. An underground explorer robot based on peristaltic crawling of earthworms. Ind Rob 2009;36:358–364.
16. Onal CD, Wood RJ, Rus D. An origami-inspired approach to worm robots. IEEE ASME Trans Mechatron 2013;18: 430–438.
17. Fang H, Zhang Y, Wang KW. An earthworm-like robot using origami-ball structures. In: Active and Passive Smart Structures and Integrated Systems 2017. Portland, OR: International Society for Optics and Photonics, April 2017:1016414.
18. Tanaka Y, Ito K, Nakagaki T, *et al.* Mechanics of peristaltic locomotion and role of anchoring. J R Soc Interface 2012;9: 222–233.
19. Liljebäck P, Pettersen KY, Stavdahl Ø, *et al.* A review on modelling, implementation, and control of snake robots. Rob Auton Syst 2012;60:29–40.
20. Alexander RM. Principles of Animal Locomotion. Princeton, NJ: Princeton University Press, 2003.
21. Tang W, Xie S, Li H, *et al.* The influence of lifting behavior on energy efficiency in rectilinear locomotion. Arch Appl Mech 2017;87:1–13.
22. Marvi H, Bridges J, Hu DL. Snakes mimic earthworms: propulsion using rectilinear travelling waves. J R Soc Interface 2013;10:20130188.
23. Boxerbaum AS, Chiel HJ, Quinn RD. A new theory and methods for creating peristaltic motion in a robotic platform. In: 2010 IEEE International Conference on Robotics and Automation (ICRA). IEEE, pp. 1221–1227, May 2010.
24. Kandhari A, Horchler AD, Zucker GS, *et al.* Sensing contact constraints in a worm-like robot by detecting load anomalies. In: Conference on Biomimetic and Biohybrid Systems. Cham, Switzerland: Springer, pp. 97–106, July 2016.
25. Kandhari A, Stover MC, Jayachandran PR, *et al.* Distributed sensing provides a soft worm robot feedback on its environment and internal state. 2018 Conference on Biomimetic and Biohybrid Systems. Paris, France: Springer, July 2018: 236–248.

26. Aydin YO, Molnar JL, Goldman DI, *et al.* Design of a soft robophysical earthworm model. IEEE RoboSoft 2018, Livorno, Italy.
27. Kandhari A, Daltorio KA. A kinematic model to constrain slip in soft body peristaltic locomotion. IEEE RoboSoft 2018, Livorno, Italy.
28. Omori H, Hayakawa T, Nakamura T. Locomotion and turning patterns of a peristaltic crawling earthworm robot composed of flexible units. In: 2008 IEEE/RSJ International Conference on Intelligent Robots and Systems. Nice, France: IEEE, September 2008:1630–1635.
29. Mirletz BT, Bhandal P, Adams RD, *et al.* Goal-directed CPG-based control for tensegrity spines with many degrees of freedom traversing irregular terrain. Soft Robot 2015;2: 165–176.
30. Gong C, Travers MJ, Astley HC, *et al.* Kinematic gait synthesis for snake robots. Int J Rob Res 2016;35:100–113.
31. Transeth AA, Leine RI, Glocker C, *et al.* Snake robot obstacle-aided locomotion: modeling, simulations, and experiments. IEEE Trans Robot 2008;24:88–104.
32. Liljeback P, Pettersen KY, Stavdahl Ø, *et al.* Experimental investigation of obstacle-aided locomotion with a snake robot. IEEE Trans Robot 2011;27:792–800.
33. Zimmermann K, Zeidis I. Worm-like locomotion as a problem of nonlinear dynamics. J Theor Appl Mech 2007; 45:179–187.
34. Zarrouk D, Shoham M. Analysis and design of one degree of freedom worm robots for locomotion on rigid and compliant terrain. J Mech Des 2012;134:021010.
35. Huang Y, Kandhari A, Chiel HJ, *et al.* Slip reduction controls of mesh-body worm robot developed from a mathematical model. IEEE ROBIO 2017. Macau, China: IEEE, December 2017:1474–1479.
36. Adams W, Sridar S, Thalman CM, *et al.* Water Pipe robot utilizing soft inflatable actuators. IEEE RoboSoft 2018, Livorno, Italy.
37. Andersen K. A nitinol actuated worm-inspired robot capable of forward motion, turning, and climbing obstacles. Masters Thesis. Cleveland, OH: Case Western Reserve University, 2017.
38. Huang Y, Kandhari A, Chiel HJ, *et al.* Mathematical modeling to improve control of mesh body for peristaltic locomotion. In: Conference on Biomimetic and Biohybrid Systems. Cham, Switzerland: Springer, pp. 193–203, July 2017.
39. Chirikjian GS, Burdick JW. The kinematics of hyper-redundant robot locomotion. IEEE Trans Rob Autom 1995; 11:781–793.
40. Zhang Z, Zheng L, Yu J, *et al.* Three recurrent neural networks and three numerical methods for solving a repetitive motion planning scheme of redundant robot manipulators. IEEE ASME Trans Mechatron 2017;22: 1423–1434.
41. Yuan J. Hierarchical motion planning for multisteering tractor–trailer mobile robots with on-axle hitching. IEEE ASME Trans Mechatron 2017;22:1652–1662.
42. Aguilar J, Zhang T, Qian F, *et al.* A review on locomotion robophysics: the study of movement at the intersection of robotics, soft matter and dynamical systems. Rep Prog Phys 2016;79:110001.

Address correspondence to:
Akhil Kandhari
Flexible Robotics Laboratory
Department of Mechanical and Aerospace Engineering
Case Western Reserve University
Glennan Building, Room 864
10900 Euclid Avenue
Cleveland, OH 44106-7222

E-mail: akhil.kandhari@case.edu